Received: 5 April 2019 | Revised: 1 July 2019 | Accepted: 7 August 2019 | Published on: 17 September 2019

DOI: 10.1002/gamm.202000008

ORIGINAL PAPER

3D phase field simulations of ductile fracture

Timo Noll[1,2] | **Charlotte Kuhn**[1] | **Darius Olesch**[1,2] | **Ralf Müller**[2]

[1]Computational Mechanics, Technische Universität Kaiserslautern, Kaiserslautern, Germany

[2]Institute of Applied Mechanics, Technische Universität Kaiserslautern, Kaiserslautern, Germany

Correspondence
Timo Noll, Computational Mechanics, Technische Universität Kaiserslautern, Gottlieb-Daimler-Straße, 67663 Kaiserslautern, Germany.
Email: tnoll@rhrk.uni-kl.de

Funding information
Deutsche Forschungsgemeinschaft

Abstract

In this contribution a phase field model for ductile fracture with linear isotropic hardening is presented. An energy functional consisting of an elastic energy, a plastic dissipation potential and a Griffith type fracture energy constitutes the model. The application of an unaltered radial return algorithm on element level is possible due to the choice of an appropriate coupling between the nodal degrees of freedom, namely the displacement and the crack/fracture fields. The degradation function models the mentioned coupling by reducing the stiffness of the material and the plastic contribution of the energy density in broken material. Furthermore, to solve the global system of differential equations comprising the balance of linear momentum and the quasi-static Ginzburg-Landau type evolution equation, the application of a monolithic iterative solution scheme becomes feasible. The compact model is used to perform 3D simulations of fracture in tension. The computed plastic zones are compared to the dog-bone model that is used to derive validity criteria for K_{IC} measurements.

KEYWORDS

dog-bone model, ductile fracture, fine element, phase field model

1 | INTRODUCTION

Before a material fails it can sustain external loads by deforming itself in such a way, that once the external loads are withdrawn, it does not return to its initial shape, that is, the material performs a plastic transformation. Dependent on how strong the capability of a material to perform a plastic transformation is developed, different theories have to be employed to describe the failure process of the respective material. From an engineering point of view however, generalized failure parameters are often of greater interest than the actual failure mechanism. Thus, for example, validity criteria for CT-specimen that have to be met in tensile testing exist to measure a valid fracture toughness K_{IC}. These criteria shall guarantee that assumptions of small scale yielding and linear fracture mechanics are fulfilled as well as a state of plane strain dominates at the crack tip. The latter assumption is based on the so called "dog-bone" model, predicting a state of plane strain in the center of the specimen and a plane stress state at the surface. However, the validity of the criteria is frequently questioned.[1,2]

Assessing failure of ductile materials by means of numerical simulations has been proved to be difficult so far. The concept of J-integrals, where, analogously to the K-concept in linear elastic fracture mechanics, the parameter J is a measure for

the load exerted by the surrounding material on the process zone, is widely used in industrial applications, but exhibits certain drawbacks. It cannot model the nucleation of new cracks, and thus, relies on preexisting cracks. Furthermore, J_C is not an intrinsic material parameter, but dependent on geometry of the specimen and, thus, can hardly be applied to complex structures, such as welds.[3] Concerning fracture simulations within the finite element method another challenge is the tracking of fractures since displacement jumps across crack faces have to be addressed by special algorithmic treatment. Such treatments comprise on the one hand remeshing techniques, where the finite element mesh is adapted frequently to the new crack topology and on the other hand techniques like the extended finite element method (XFEM), where a discontinuous function and the two dimensional asymtotic crack tip displacement field are added to the displacement based FE approximation in 3D.[4,5] However, these approaches still require either the *a priori* knowledge of the crack path or the introduction of additional failure criteria.

In contrast to the aforementioned discrete approaches towards fracture, diffuse modeling approaches relying on a phase field formulation are conceptually different and can overcome shortcomings of the former. In phase field models a scalar valued order parameter is employed to distinguish between different phases. Each phase is assigned to a certain value of the phase field parameter. Within the phases the phase field parameter is constant. The transition between two phases is modeled by a diffuse transition zone, where the phase field parameter interpolates smoothly between the values assigned to the adjoining phases. The constitutive equation and the gradient type evolution equations of the underlying model are determining the evolution of the phase field parameter such that the interfaces between the phases evolve naturally, rendering the tracking of interfaces unnecessary as transition conditions between the phases are fulfilled automatically. In the context of fracture mechanics distinct values of the phase field parameter are associated to intact and fractured material, respectively. The different phases evolve such that cracks are modeled as lines/surfaces in 3D. The formal foundation of the phase field models for fracture originating from the mechanics community arises from the variational formulation for brittle fracture by Francfort and Marigo[6] which was regularized by Bourdin.[7] In case of brittle fracture an appropriate energy functional consisting of an elastic energy contribution and a Griffith type fracture energy provides the coupling between the displacement field and the phase field fracture parameter. The solution of the coupled system of equations comprising a Ginzburg-Landau type evolution equation and the balance of momentum determines the evolution of fracture. Due to the implicit modeling of cracks by a continuous field coupling discontinuities in the displacement field occur, thus, rendering the explicit tracking of crack interfaces unnecessary and enable a straightforward implementation in the FE framework. This is particularly beneficial in the context of plasticity, where the transfer of plastic variables during the remeshing procedure has been proved to be a demanding task.[8] Phase field modeling of quasi-static brittle fracture has been target of intensive research in recent years[7,9–14] and is well established today. Dynamic brittle fracture has been studied.[15,16] Attempts towards ductile dynamic fracture were undertaken by Hofacker and Miehe[17] and Ulmer and Hofacker.[18] A phase field model for brittle fracture in elastic-plastic solids where the evolution of the fracture field is driven by elastic strains only has been proposed by Duta et al.[19] A phase field fracture model is combined with a thermal softening shear band model.[20] Ambati et al. proposed a ductile fracture model where an elaborated degradation function accomplishes the coupling between fracture field and strains such, that an adjustment of the model parameters allows for good reproduction of experimental data. Due to the chosen coupling a computationally expensive staggered scheme is required to solve the coupled system of equations.[21] A model using a combination of a cubic degradation function providing a stress-strain response prior to crack initiation that approximates more accurately the linear elastic behavior and a yield surface degradation function different from the degradation function of the elastic energy is presented.[22]

In the ductile phase field model[23] the same quadratic degradation function for the elastic energy and the plastic dissipation potential is used. By using the same degradation function the handling of the numerics is greatly alleviated. However, the usage of a quadratic degradation function renders a reinterpretation of the plastic parameters necessary, thus, the model is enhanced in this contribution. As the application of a quadratic function leads to degradation prior to the onset of plastic deformation the combination of a cubic degradation function is used instead. Due to its manageable amount of material parameters which allow a clear interpretation with respect to experimentally measurable fracture mechanical and elastic-plastic material parameters, this model is used to investigate the size and shape of the plastic zone for specimen under tensile loading in 3D. In Section 2 the ductile phase field model is sketched. Subsequently, it is investigated how the model can describe the plastic deformation along the crack front in a single notched specimen of varying thickness under tensile loading compared to the dog-bone model and numerical simulations performed with classical approaches. The numerical results comprising the quest for suitable finite element meshes and the fracture simulations in 3D are presented in Section 3. Some concluding remarks are given in Section 4.

2 | DUCTILE PHASE FIELD FRACTURE MODEL

2.1 | Elastic phase field model

As the ductile phase field fracture model represents an extension to the elastic phase field fracture formulation, the latter is introduced at first. The potential energy

$$\Psi(\boldsymbol{\varepsilon}, s) = \underbrace{g(s) W_{\mathrm{el}}(\boldsymbol{\varepsilon})}_{=\Psi_{\mathrm{el}}} + \underbrace{\mathcal{G}_c \left(\frac{1}{4\epsilon}(1-s)^2 + \epsilon |\nabla s|^2 \right)}_{=\Psi_{\mathrm{fr}}}, \tag{1}$$

forms the basis of the model with the elastic strain energy given by

$$W_{\mathrm{el}}(\boldsymbol{\varepsilon}^{\mathrm{e}}) = \frac{1}{2} \boldsymbol{\varepsilon}_{\mathrm{el}} : (\mathbb{C} \boldsymbol{\varepsilon}^{\mathrm{e}}). \tag{2}$$

The potential consists of two parts: an elastic part Ψ_{el} and a fracture part Ψ_{fr}. The elastic strain energy, where $\boldsymbol{\varepsilon}^{\mathrm{e}}$ is the small strain tensor and $\mathbb{C}$ the fourth-order stiffness tensor, is subject to the degradation function $g(s)$, where s represents the fracture field accounting for the loss of stiffness in fractured material. The value $s = 1$ indicates an intact material, while $s = 0$ represents broken material. The stiffness tensor is assumed to be isotropic throughout this contribution. The choice of the degradation function $g(s)$ is discussed in Section 2.2. The fracture surface energy is represented by Ψ_{fr}. The parameter $\mathcal{G}_c$ is the fracture resistance and can be related to the fracture toughness. The length parameter ϵ describes not only the width of the transition zone between fractured and intact material, but can be also related together with $\mathcal{G}_c$ and the elastic stiffness to a fracture stress in homogeneous stress states.[7,24] It is thus decisive for crack nucleation. The stress is derived from the potential by

$$\boldsymbol{\sigma} = \frac{\partial \Psi}{\partial \boldsymbol{\varepsilon}} = g(s) \mathbb{C} \boldsymbol{\varepsilon}. \tag{3}$$

The balance of linear momentum is given by

$$\mathrm{div} \boldsymbol{\sigma} = \mathbf{0}, \tag{4}$$

where volume forces have been neglected. The time dependent Ginzburg-Landau equation describes the evolution of the fracture field by relating the rate of s to the variational derivative of the potential

$$\dot{s} = -M \frac{\delta \Psi}{\delta s} = M \left[2\mathcal{G}_c \epsilon \Delta s - g'(s) W_{\mathrm{el}}(\varepsilon^{\mathrm{e}}) + \frac{\mathcal{G}_c}{2\epsilon}(1-s) \right]. \tag{5}$$

2.2 | Plastic phase field model

In contrast to the elastic phase field fracture model, in the ductile model the total strain $\boldsymbol{\varepsilon}$ is not identical to the elastic strain

$$\boldsymbol{\varepsilon}^{\mathrm{e}} = \boldsymbol{\varepsilon} - \boldsymbol{\varepsilon}^{\mathrm{p}}. \tag{6}$$

Furthermore a plastic dissipation contribution

$$\Pi_{\mathrm{pl}} = \left(\sigma_Y + \frac{1}{2} H \alpha \right) \alpha \tag{7}$$

is added to the potential, where α is the hardening variable accounting for the accumulated plastic strain. The parameter σ_{Y} and H represent the initial yield stress and the linear isotropic hardening modulus. The coupling of plastic deformation to the crack field is accomplished by the degradation function. A parameterized cubic degradation function

$$g(s) = \beta(s^3 - s^2) + 3s^2 - 2s^3 + \eta \tag{8}$$

suggested by Borden et al.[22] is used, where η is the residual stiffness, introduced for numerical reasons. The parameter β can vary between 0 and 2, where $\beta = 2.0$ yields the common quadratic degradation function found in many phase field fracture approaches. The benefit of a cubic degradation function with $\beta = 0$ will be illustrated by a discussion of a 1D bar under tensile

loading in Section 2.3. Two solutions for the fracture variable s exist, one with $s \neq 0$, represented by the green curve, and a second one with $s = 1$, represented by the blue curve, corresponding to intact material. As initially, that is, for small loading, only the second solution is admissible, the linear stress-strain relation is recovered, thus no degradation occurs and a differentiation between effective and nominal elastic plastic parameters as conducted by Kuhn et al.[23] becomes unnecessary. Taking the modification outlined above into account the elastic-plastic potential becomes

$$\Psi(\boldsymbol{\varepsilon}, s; \boldsymbol{\varepsilon}^{\mathrm{p}}, \alpha) = g(s) W_{\mathrm{el}}(\boldsymbol{\varepsilon} - \boldsymbol{\varepsilon}^{\mathrm{p}}) + \underbrace{g(s)\left(\sigma_{\mathrm{Y}} + \frac{1}{2} H \alpha\right) \alpha}_{\Pi_{\mathrm{pl}}} + \mathcal{G}_c \left(\frac{1}{4\epsilon}(1-s)^2 + \epsilon |\nabla s|^2 \right) \tag{9}$$

with

$$W_{\mathrm{el}}(\boldsymbol{\varepsilon} - \boldsymbol{\varepsilon}^{\mathrm{p}}) = \frac{1}{2}(\boldsymbol{\varepsilon} - \boldsymbol{\varepsilon}^{\mathrm{p}}) : [\mathbb{C}(\boldsymbol{\varepsilon} - \boldsymbol{\varepsilon}^{\mathrm{p}})] \tag{10}$$

The stress is computed analogously to the elastic model, but with taking (6) into account becomes

$$\boldsymbol{\sigma} = \frac{\partial \Psi}{\partial \boldsymbol{\varepsilon}} = g(s) \mathbb{C}(\boldsymbol{\varepsilon} - \boldsymbol{\varepsilon}^{\mathrm{p}}). \tag{11}$$

The balance of linear momentum (4) remains unaltered. The Ginzburg-Landau equation derived from the elastic-plastic potential (9) reads

$$\begin{aligned} \dot{s} &= -M \frac{\delta \Psi}{\delta s} \\ &= M \left[2\mathcal{G}_c \epsilon \Delta s - g'(s) \left(W(\boldsymbol{\varepsilon} - \boldsymbol{\varepsilon}^{\mathrm{p}}) + \left(\sigma_{\mathrm{Y}} + \frac{1}{2} H \alpha \right) \alpha \right) + \frac{\mathcal{G}_c}{2\epsilon}(1-s) \right]. \end{aligned} \tag{12}$$

Thus, the fracture field is not only driven by elastic strains, but also by the accumulated plastic strain α. In von Mises plasticity it is assumed, that only the deviatoric part of the the strain is subject to plastic deformation. The deviatoric parts of the stress, the elastic and the plastic strain quantities are

$$\boldsymbol{s} = \mathrm{dev}(\boldsymbol{\sigma}), \qquad \boldsymbol{e} = \mathrm{dev}(\boldsymbol{\varepsilon}), \qquad \text{and} \qquad \boldsymbol{e}^{\mathrm{p}} = \mathrm{dev}(\boldsymbol{\varepsilon}^{\mathrm{p}}) \tag{13}$$

respectively, where the deviator is defined as $\mathrm{dev}(\cdot) = (\cdot) - \frac{1}{3}\mathrm{tr}(\cdot)\mathbb{1}$, with $\mathrm{tr}(\cdot)$ indicating the trace of $(\cdot)$ and $\mathbb{1}$ the unity tensor. Plastic material behavior is characterized by the von Mises type yield criterion stating

$$f(\boldsymbol{s}, \alpha) = \|\boldsymbol{s}\| + \sqrt{\frac{2}{3}}\, q = 0, \tag{14}$$

where

$$q = -\frac{\partial \Psi}{\partial \alpha} = -g(s)(\sigma_{\mathrm{Y}} + H\alpha) \tag{15}$$

is the driving force for the plastic deformation. As isotropic material behavior is considered throughout this contribution, the relation between deviatoric stress and strain is

$$\boldsymbol{s} = g(s) 2\mu(\boldsymbol{e} - \boldsymbol{e}^{\mathrm{p}}), \tag{16}$$

where μ is the shear modulus or second Lamé constant. With (13), (16), and (15) the yield criterion states

$$f(\boldsymbol{s}, \alpha) = g(s)\|2\mu(\boldsymbol{e} - \boldsymbol{e}^{\mathrm{p}})\| - g(s)\sqrt{\frac{2}{3}}(\sigma_{\mathrm{Y}} + H\alpha) = 0. \tag{17}$$

By choosing the same degradation function for the elastic potential W_{el} and the plastic contribution Π_{pl} in (9) it is feasible to formulate an undegraded counterpart of the yield criterion

$$f^*(\boldsymbol{s}^*, \alpha) = \|\boldsymbol{s}^*\| - \sqrt{\frac{2}{3}}(\sigma_{\mathrm{Y}} + H\alpha) = 0, \tag{18}$$

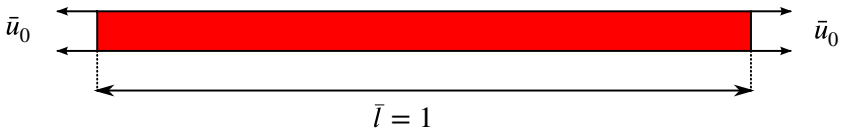

FIGURE 1 Sketch of a 1D bar under tensile loading

with the undegraded counterpart of the stress deviator $\boldsymbol{s}^*$. The undegraded counterpart of the yield function does not depend on the fracture field and thus allows for direct application of the usual "radial return"-algorithm for plasticity.[25]

2.3 | 1D problem

In order to illustrate some features of the model the case of a 1D bar under linear increasing tensile loading as depicted in Figure 1 shall be briefly discussed.

In the quasi-static case and if $M \to \infty$ for the homogeneous solution of the fracture field the relation

$$g(s)'(W_{\text{el}} + \Pi_{\text{pl}}) - \mathcal{G}_c \frac{1-s}{2\epsilon} = 0 \tag{19}$$

holds. If the parameters of the degradation function are chosen $\beta = 0$ and $\eta = 0$, dependent on whether the yield stress is already reached or not the sum of the undegraded elastic energy and the plastic dissipation contribution is given by

$$W_{\text{el}} + \Pi_{\text{pl}} = \begin{cases} \frac{1}{2} E \boldsymbol{\varepsilon}_0^2 & \text{if } \boldsymbol{\varepsilon}_0 \leq \frac{\sigma_{\text{Y}}}{H} \\ \frac{1}{2} E \left(\boldsymbol{\varepsilon}_0^2 - \frac{E}{E+H} \left(\boldsymbol{\varepsilon}_0 - \frac{\sigma_{\text{Y}}}{H} \right)^2 \right) & \text{if } \boldsymbol{\varepsilon}_0 > \frac{\sigma_{\text{Y}}}{H}. \end{cases} \tag{20}$$

Two solutions for the fracture field are obtained from Equation (19) in dependence of $W_{\text{el}} + \Pi_{\text{pl}}$,

$$s_1 = 1, \tag{21}$$

$$s_2 = \frac{\mathcal{G}_c}{12\varepsilon(W_{\text{el}} + \Pi_{\text{pl}})}, \tag{22}$$

where s_2 is only admissible (ie, $s_2 \leq 1$) if $W_{\text{el}} + \Pi_{\text{pl}} > \frac{\mathcal{G}_c}{12\epsilon}$. For $W_{\text{el}} + \Pi_{\text{pl}} > \frac{\mathcal{G}_c}{12\epsilon}$ the degraded solution s_2 is energetically favorable compared to s_1, which corresponds to the solution for intact material. By setting $s_2 = 1$ in the second solution of Equation (21) the critical strain for the onset of degradation

$$\boldsymbol{\varepsilon}_s = \sqrt{\frac{E+H}{EH} \left(\frac{\sigma_{\text{Y}}^2}{H} + \frac{1}{6} \frac{\mathcal{G}_c}{\epsilon} \right)} - \frac{\sigma_{\text{Y}}}{H} \tag{23}$$

is obtained. For the undegraded stress σ^*

$$\sigma^* = \begin{cases} E \boldsymbol{\varepsilon}_0 & \text{if } \boldsymbol{\varepsilon}_0 \leq \frac{\sigma_{\text{Y}}}{H} \\ \frac{EH}{E+H} \left(\boldsymbol{\varepsilon}_0 + \frac{E}{H} \frac{\sigma_{\text{Y}}}{H} \right) & \text{if } \boldsymbol{\varepsilon}_0 > \frac{\sigma_{\text{Y}}}{H} \end{cases} \tag{24}$$

holds. The local maximum of the stress, corresponding to the fracture stress is obtained by

$$\frac{\mathrm{d}}{\mathrm{d}\boldsymbol{\varepsilon}_0} (g(s)\sigma^*) = 0. \tag{25}$$

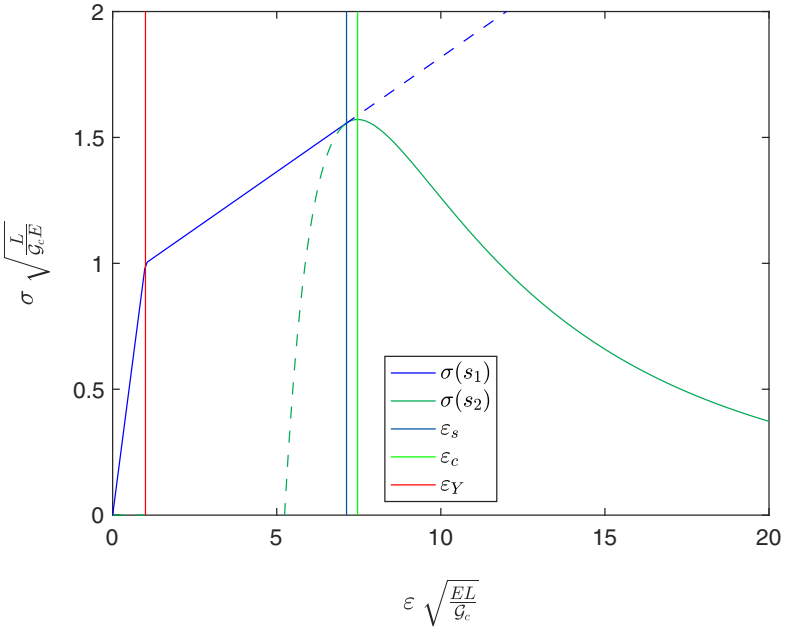

FIGURE 2 Stress-strain curve of a 1d bar under tensile loading

TABLE 1 Material, geometry and loading properties used in the simulations. The relation of the non-dimensional quantities to E, $\mathcal{G}_c$, l, and T correspond to dimensionless model by Kuhn et al.[23]

Poisson's ratio, ν	0.25
Regularization length, ϵ	$0.02l$
Residual stiffness, η	10^{-4}
Deg. fct. parameter, β	10^{-6}
Mobility constant, M	$10\ \frac{l}{\mathcal{G}_c T}$
Length, l	$1.0l$
Hardening modulus, H	$0.1E$
Yield stress, σ_Y	$1.0\ \sqrt{\frac{\mathcal{G}_c E}{l}}$
Loading rate, u_0^*	$1.0\ \sqrt{\frac{\mathcal{G}_c l}{E}}$

From Equation (25) an expression for the fracture strain in case of elastic-plastic failure

$$\boldsymbol{\varepsilon}_c = \sqrt{\frac{1}{3}\frac{E+H}{EH}\left[\left(\frac{\sigma_Y^2}{H}+\frac{5}{18}\frac{\mathcal{G}_c}{\epsilon}\right)+\sqrt{4\left(\frac{\sigma_Y^2}{H}\right)^2+\frac{8}{9}\frac{\sigma_Y^2\mathcal{G}_c}{H\epsilon}+\frac{25}{324}\left(\frac{\mathcal{G}_c}{\epsilon}\right)^2}\right]}-\frac{\sigma_Y}{H} \tag{26}$$

is obtained. The resulting stress-strain curve is depicted in Figure 2. Until the loading reaches the initial yield fracture load $\boldsymbol{\varepsilon}_0 = \boldsymbol{\varepsilon}_Y = \frac{\sigma_Y}{H}$ the elastic stress-strain relation is linear and merges to the less steep, however still linear, elastic-plastic regime, described by the continuous blue line, representing the stress field for solution s_1. When the load $\boldsymbol{\varepsilon}_0 = \boldsymbol{\varepsilon}_s$ is reached, indicated by the vertical blue line, s_2 becomes admissible and the stress-strain relation is described by the continuous green curve from that point on. The maximum value of the stress is reached at $\boldsymbol{\varepsilon}_0 = \boldsymbol{\varepsilon}_c$, denoted by vertical line in green.

3 | NUMERICAL RESULTS

The numerical simulations presented in this section were performed within the finite element framework FEAP on a cluster comprising 8 AMD Opteron 6140 8 core nodes at 64 GB RAM. An implicit time integration scheme is applied to solve the

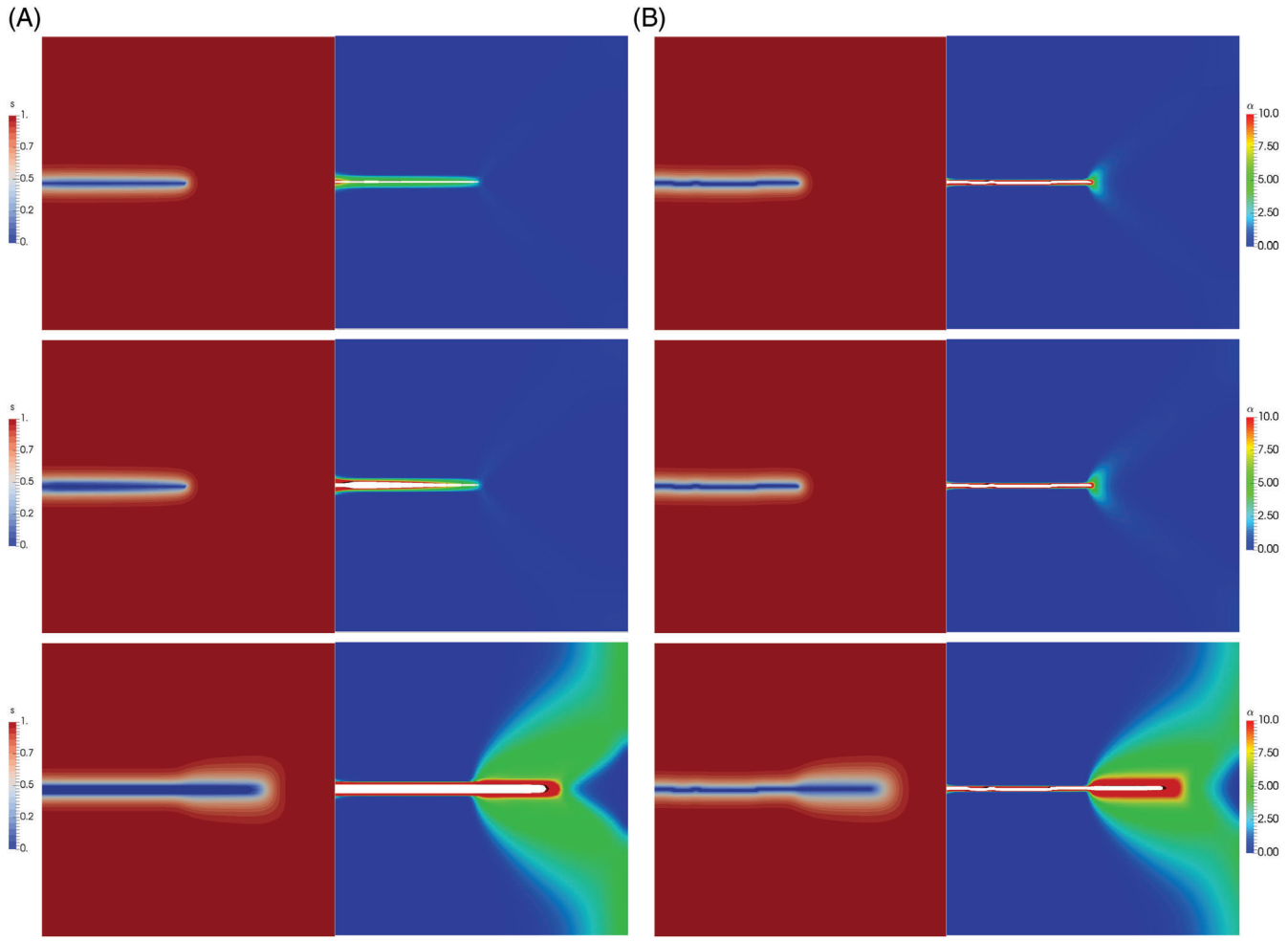

FIGURE 3 Fracture field (left) and hardening variable (right) for simulations with an $80 \times 80 \times 1$ (A) and an $200 \times 200 \times 1$ (B) uniform mesh from bottom to top

weak forms of (4) and (12) discretized in time and space on the global level. The plastic updates are performed on local level where a "radial-return" algorithm,[25] convenient in numerical plasticity, is applied. A monolothic Newton-Raphson solution strategy is chosen for the solution of the non-linear global system of equations in $\boldsymbol{u}$ and s. If necessary a line-search procedure is invoked. Dependent on the number of Newton iterations needed to meet the convergence criterion, the time step size is increased or decreased, respectively. Healing of fractured material is prevented by fixing nodes where the fracture field drops below a small threshold value ($s \leq 10^{-8}$) to zero and corresponding nodal values are canceled from the global system of equations.

In order to perform 3D simulations in an efficient way, an appropriate finite element mesh is needed. As a reference the domain of a quadratic single notched tension probe of edge length l and thickness $d = l/10$ depicted in Figure 6 on the right is discretized in $200 \times 200 \times 1$ eight node brick elements. The initial crack is generated by prescribing the initial condition $s = 0$ from $x_1 = -l/2$ to $x_1 = 0$ in the plane, where $x_2 = 0$. A linear increasing normal tensile loading u^* on the bottom and top of the specimen with

$$u^* = 0.5 \cdot t \cdot u_0^* \tag{27}$$

is applied to enable stable crack growth. The mobility constant is chosen high enough to ensure quasi-static crack growth. Material geometry and loading properties are summarized in Table 1.

Any quantity mentioned in this section is a dimensionless quantity in relation to a given Youngs modulus E, a given fracture toughness $\mathcal{G}_c$, a unit length l and a unit time T.[23] However, for the sense of simplicity no extra symbol is introduced for the dimensionless quantities. Contour plots of the fracture field and the hardening variable are shown in Figure 3B at four different instances of time. With increasing load plastic deformation emerges in a 45° angle to the notch direction. Thereupon the crack

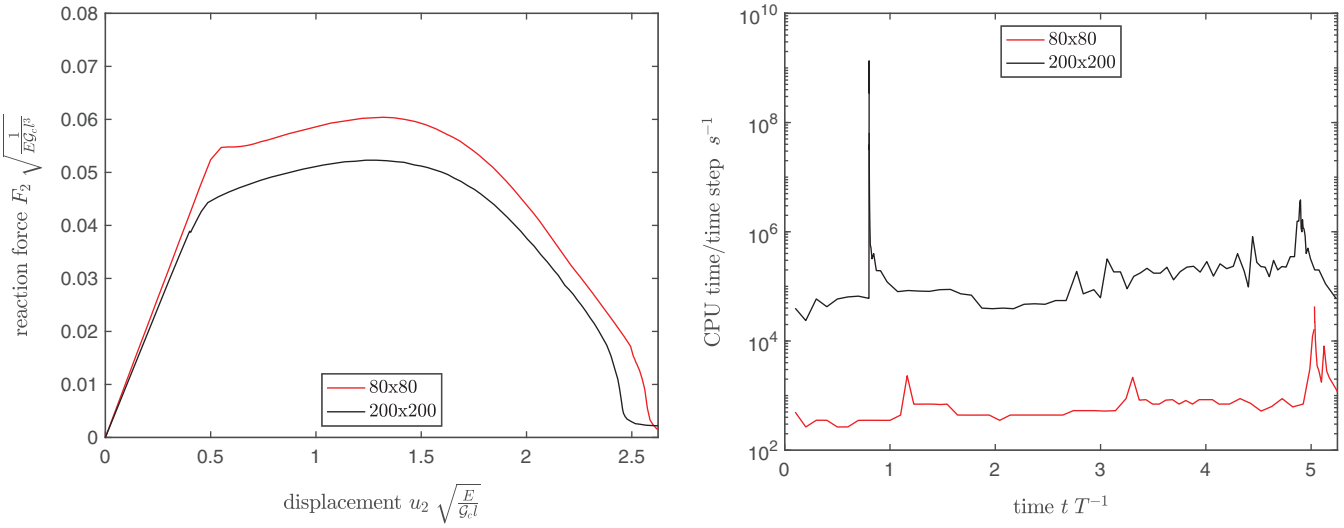

FIGURE 4 Load displacement curve, where F_2 is the reaction force acting on the initially undamaged, right part of the structures x_2-surface (left) and CPU time spent in the respective simulation time intervals for unrefined meshes (right)

TABLE 2 Simulation data of mesh convergence simulations with certain refinements prior to the cleanup step

	Mesh			Refinement				
No.	**Base**	**Elements**	**Nodes**	d_r	w	**Elmt. size**	**degree**	**Trans. elmts**
1	200×200	40 000	80 802	0	0	$0.005l$	0	0
2	20×20	4560	9242	$0.1l$	2	$0.0056l$	2	640
3	40×40	2720	5614	$0.05l$	2	$0.0083l$	1	80
4	40×40	3360	6902	$0.1l$	4	$0.0083l$	1	80
5	40×40	5920	12 504	$0.2l$	6	$0.0083l$	1	80
6	80×80	12 480	25 318	$0.1l$	8	$0.0042l$	1	160

field drops slightly in the first instance in the same direction, while the crack eventually grows in straight direction. However, the initial drop of the crack field remains and causes the widened profile of the crack.

A comparison of the respective fields with a simulation on a $80\times80\times1$ (see Figure 3) mesh yields a smaller crack width and stronger pronounced plastic zone in case of the $200\times200\times1$ mesh. Furthermore, the load-bearing capacity of the structure is overestimated in the simulation with the coarser mesh, see Figure 4. An adjustment of the fracture toughness $\mathcal{G}_c$ in order to keep the total energy in the system for the modified ratio $\frac{h_e}{\varepsilon}$ as proposed by Bourdin and Frankfort,[26] was not conducted, since in the dimensionless description applied here the relation between other parameters, that were assumed to be given, would have been influenced. Thus, a higher peak force of the $80\times80\times1$ mesh compared to the finer mesh is expected as a result of the higher effective $\mathcal{G}_c$ for larger h_e. According to Miehe et al.[9] a ratio of $\frac{h_e}{\varepsilon}=0.5$ between element size h_e and the regularization length ε is required to resolve the regularized crack surface. This requirement is fulfilled only in case of the finer mesh, which in turn is very demanding in terms of computational effort. Thus, for the simulations in which a finer disrcetization in the x_3-direction is desired a more feasible mesh with finer parts only in the regions where the crack propagates is needed.

3.1 | In plane refinement

Five different refined meshes listed in Table 2 were tested in terms of resembling the $200\times200\times1$ mesh and their numerical efficiency. The region in the center of the domain, where the crack is expected to grow, is refined.

The refined meshes were generated by the strategy sketched in Figure 5. In the first step, the elements marked in green are refined by a factor of three, and in order to preserve mesh conformity, the transition elements, marked in orange, are introduced by the 3-refinement procedure.[27] Nodes attached to six edges in the plane, that is, of lateral valence of six (encircled in Figure 5 in the middle), formed in this step lead to a mesh of poor quality. Thus, in a second step a topological cleanup is performed. The

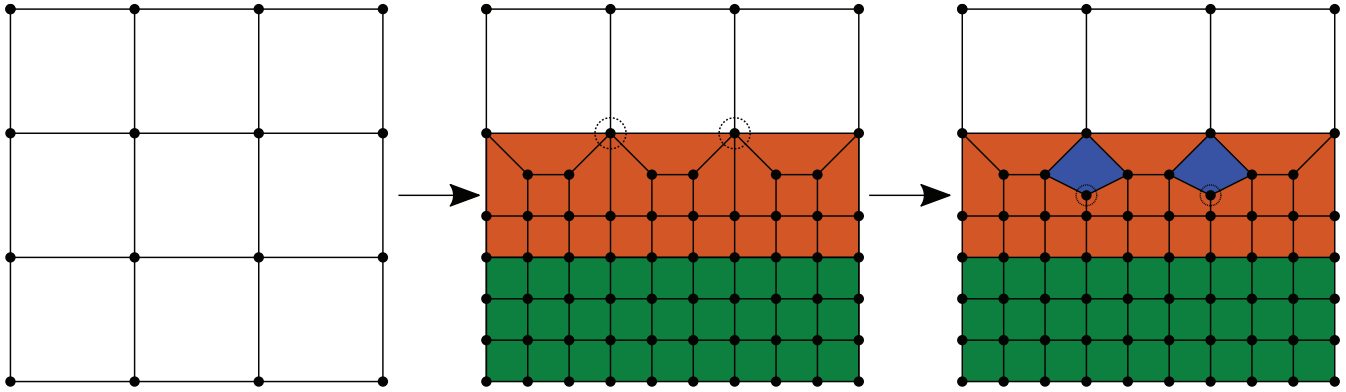

FIGURE 5 Refinement procedure: unrefined mesh on the left, refined mesh in green, transition elements in orange and the resulting nodes with valence of six circled in the middle. In blue elements created in the topological cleanup step with additional nodes circled

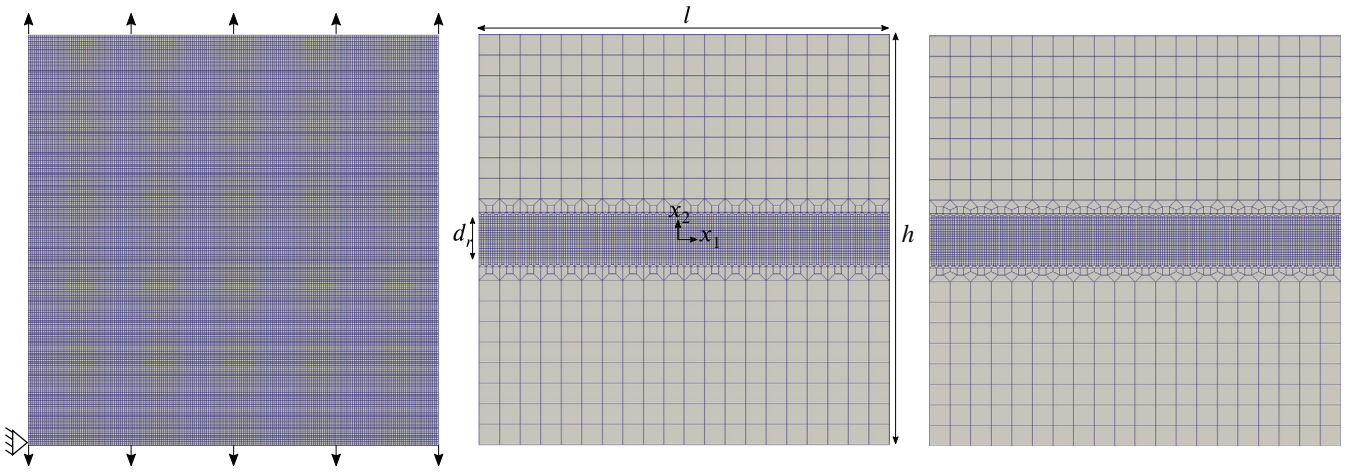

FIGURE 6 Unrefined $200 \times 200 \times 1$ mesh with boundary conditions (right), $20 \times 20 \times 1$ mesh with refinement of degree 2 without (middle) and with subsequent topological cleanup (right)

valence of the six valent nodes can be decreased by an operation called "element open." A new three valent node, encircled in Figure 5, is introduced and a new element, marked in blue, is created.[28] The refined meshes were generated with refinement templates implemented in the open source software package Blender.

The mesh density of the coarse part of the mesh and the width of the refined region d_r were varied. Mesh number 2 (Table 2) is composed of a $20 \times 20 \times 1$ base mesh and is refined by two degrees, that is, a coarse element is subdivided into nine elements, which are each subdivided into nine elements again. The width of the refined region is $d_r = 0.1l$, see Figure 6 in the middle. The mesh after subsequent topological cleanup is shown in Figure 6 on the right.

The CPU time spent to perform a simulation until the specimen is fully fractured is depicted in Figure 7 on the bottom left. Blue bars represent meshes without, while yellow bars represent meshes with a subsequent cleanup step. A comparison between the different refined meshes demonstrates that the higher the number of elements of the mesh, the higher the CPU time (c.f. Table 2). Merely mesh 2 with the coarsest unrefined mesh and highest degree of refinement does not obey to that sequence as the simulation with the respective mesh is running slower than the respective one of mesh 6 with the largest refined region. The large proportion between the number of transition elements to the total number of elements, that lead to a poorer mesh quality most likely accounts for that. The benefit of a cleanup step subsequent to the refinement step appears to depend on the respective mesh. While a strong benefit is observed for meshes 3 and 4, there is on the contrary even a slight loss in performance for mesh 2. For mesh 5 and mesh 6 the simulation failed without the subsequent topological cleanup. The CPU time spent per simulated time step is shown in Figure 7 on the bottom left for the meshes with topological cleanup. Meshes 2 and 6 with more transition elements exhibit more prominent spikes than the other meshes. Every mesh features its most prominent spike in the vicinity of simulation time $t = 1.0$, corresponding to $u_1 = 0.5$. Taking into account the load-displacement relation (see Figure 7), this instant of time is related to the transition from the linear elastic to the elastic-plastic regime. The most important result, however is, that a kink in the load-displacement curve is observed for any of the meshes emanating from the $40 \times 40 \times 1$ coarse mesh with

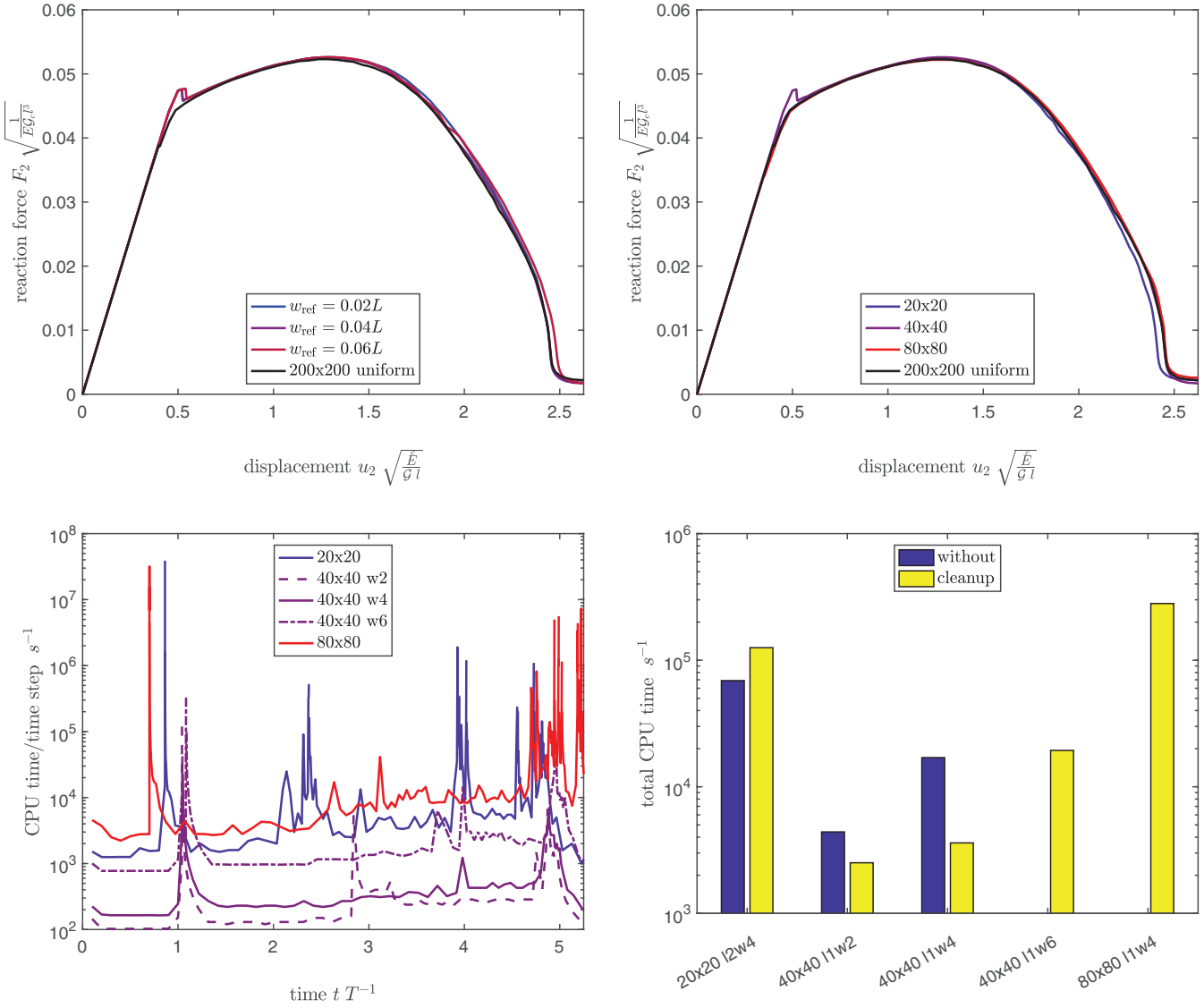

FIGURE 7 Load-displacement curves for varying width of refined region on the top left and for varying coarse mesh width on the right, where F_2 is the reaction force acting on the initially undamaged, right part of the structures x_2-surface. Distribution of CPU time with respect to the simulated time on the bottom left. Comparison CPU time spent on the full simulation for different meshes on the bottom left

only one degree of refinement. The respective kink is not present in the simulations with meshes 2 and 6. This can be explained by the fact that the element size in the refined regions of the latter two meshes is only slightly above (mesh 2) or slightly below (mesh 6) the element size of the reference mesh. Due to that qualitative distinction from the unrefined mesh, those meshes are not sufficient to be applied for the considered of problem.

3.2 | 3D tensile loading

In order to perform fracture simulations in 3D mesh 2 in the state after the performed cleanup step is chosen as template for the in plane discretization. Although, mesh 2 without the cleanup step performed superior compared to mesh 2 with the subsequent cleanup, the latter was chosen because, with regard to the other meshes the cleanup step was considered to enhance the stability of the solution scheme.

In order to evaluate a suitable out-of-plane resolution, the domain was subdivided in direction of the notch front (x_3-direction) in $n_3 = 5$ and $n_3 = 8$ elements. Apart from that the same simulation conditions were used as in the previous simulations. The accumulated plastic strain at the crack tip in direction of the crack front at $t \approx 2.8$ (corresponding $u_2 = 1.4$) is shown in Figure 8 on the right for a structure of $d = 0.4$. Independent from the discretization a symmetric profile of the accumulated plastic strain with a maximum in the center of the structure develops. The higher amount of plastic strain leading to degradation of the von

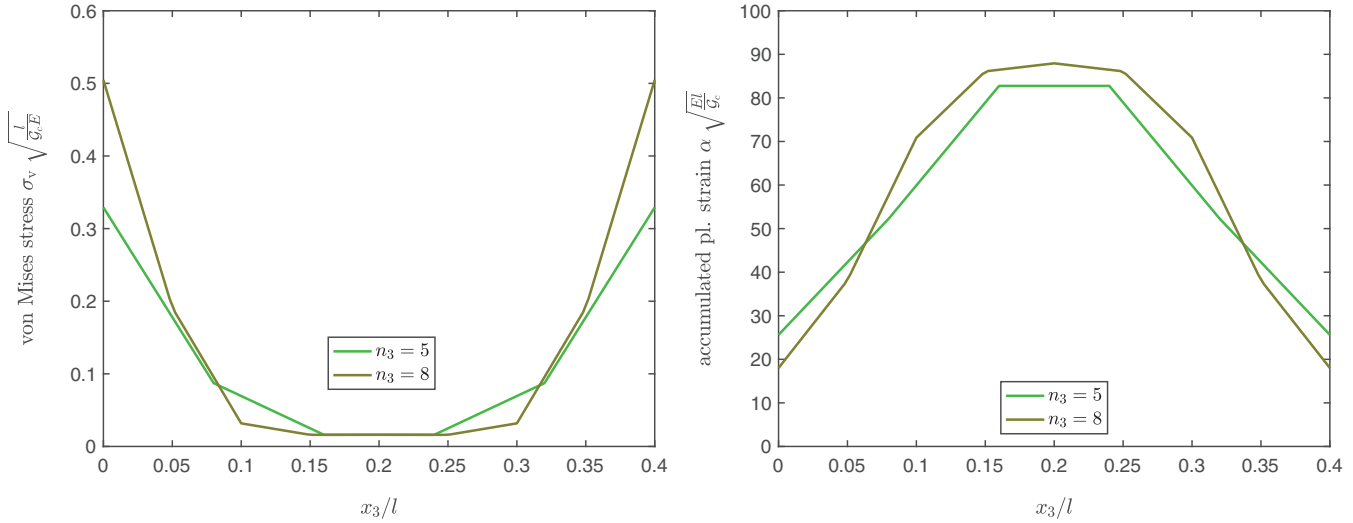

FIGURE 8 Von Mises stress (left) and accumulated plastic strain (right) at $x_1 = 0.03$ and $x_2 = 0.0$ in out-of-plane direction of the specimen with $d = 0.4$ with meshes of two different numbers of elements in x_3-direction

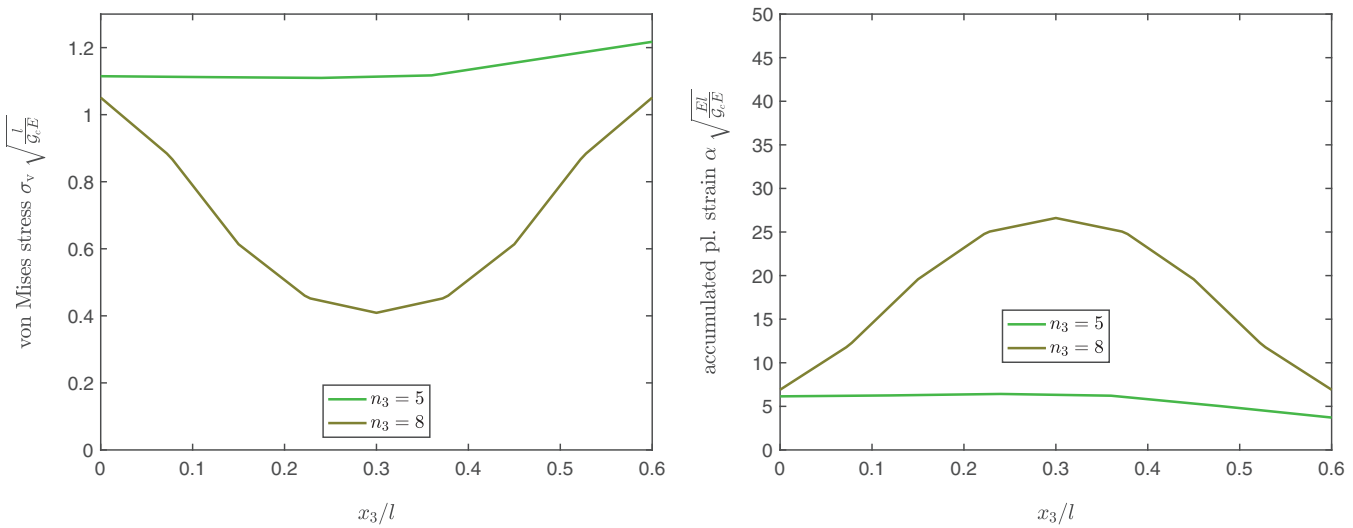

FIGURE 9 Von Mises stress (left) and accumulated plastic strain (right) at $x_1 = 0.03$ and $x_2 = 0.0$ in out-of-plane direction of the specimen with $d = 0.6$ with meshes of two different numbers of elements in x_3-direction

Mises stress in the center of the structure can be observed in Figure 8 on the left. Even if a distinct quantitative difference between the distretizations in von Mises stress at the surface of the structure is discernable, the profiles of von Mises stress and accumulated plastic strain over the whole thickness of the structure resemble each other nonetheless. Particularly in the center even the qualitative agreement is quite well. An entirely different picture emerges for a specimen with thickness of $d = 0.6$. Both, the profiles of von Mises stress and accumulated plastic strain (Figure 9) do not even agree qualitatively. Due to the insufficient disretization of only five elements in x_3-direction no symmetric profile of the accumulated plastic strain is observed and thus, also a non-symmetric profile of the von Mises stress. A comparison of the plastic zones of both discretizations in Figure 10 reveals accordingly a distinctly larger plastic zone at the surface where $z = d$. In the center of the structure the crack has already propagated further in case of the finer discretization. Supported by the observation of an enormous amount of computational time (see Figure 13 on the right) for the simulation, leads to the conclusion that a discretization in x_3-direction of 5 elements is too coarse for $d = 0.6l$.

Due to the observations described above for the following computations an out-of-plane discretization of eight elements was chosen for specimen with $d > 0.4$. The fracture field of a specimen with a thickness of $d = 0.4l$ at four instances of time is plotted in Figure 11 on the top. The four instances of time correspond to the load states illustrated in the load-displacement plot in Figure 13 on the left. While at t_1, in the linear-elastic regime, the crack front appears to be flat, a slight thumbnail

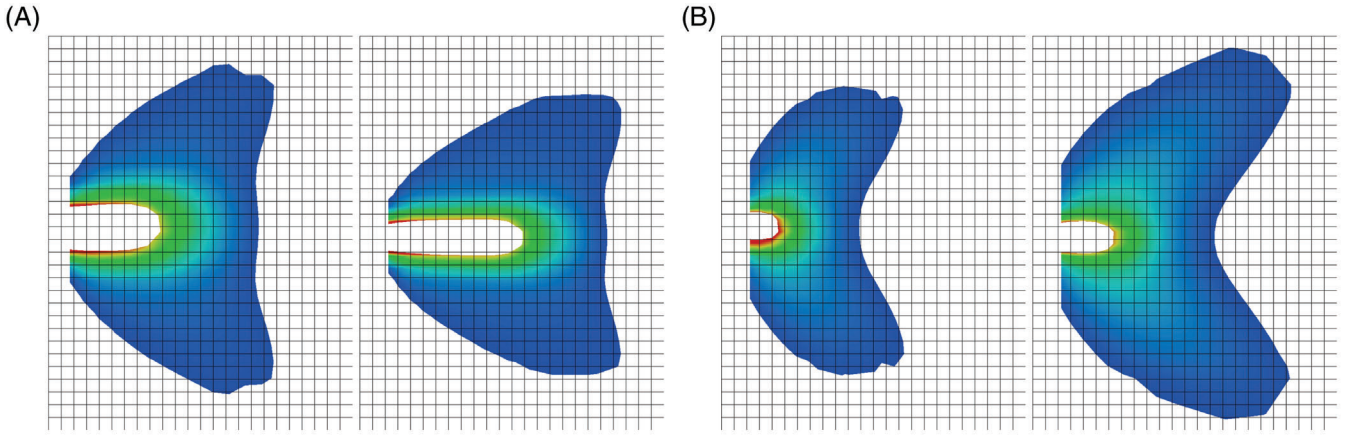

FIGURE 10 Slices of the plastic zone of the specimen with $d = 0.4$ at simulation time $t = 2.8$ (corresponding $u_2 = 1.4$) at $x_3 = d/2$ (A) and at $x_3 = d$ (B). Each plot on the left originates from a mesh with out-of-plane discretization with $n_3 = 5$ elements, the plot on the right to $n_3 = 8$

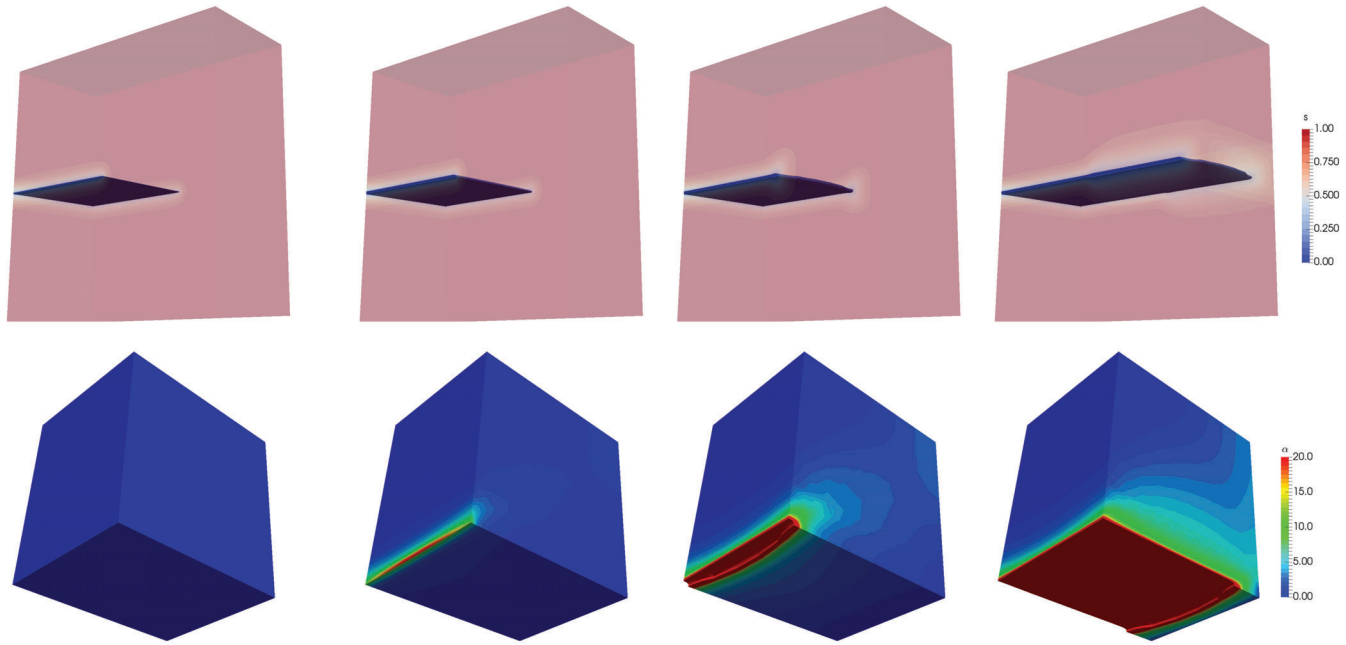

FIGURE 11 Fracture field (top) and hardening variable in the upper left quarter of the structure (bottom) at simulation time t_1, t_2, t_3, and t_4 from left to right

shape is building up after the transition to the elastic-plastic region at t_2. Around the instance when the reaction force reaches its maximum, the thumbnail shape is more pronounced (t_3) and remains at this level during the propagation of the crack front through the specimen (t_4). A widening of the transition zone between cracked and intact material in the region was the crack had propagated through compared to the pre-notched region is noticeable. The evolution of the accumulated plastic strain in the upper right quarter of the specimen is depicted in Figure 11 on the bottom. As the plastic zone is lightly developed only at t_2, a band of at least slight plastic deformation has been formed from the crack tip to the top right corner. When the crack front has propagated almost through the entire specimen at t_4 a profile of plastic deformation has been formed where the descent of plasticity becomes less steep in x_2-direction the larger the distance from the initial notch in x_1-direction.

The shape of the plastic zone is presented in Figure 12. Therefore, regions where the amount of accumulated plastic strain is very low or zero ($\alpha < 1.0\frac{\mathcal{G}_c}{El}$) are masked. Even when the amount of plastic deformation is still small at t_2, a difference in lateral extension of the plastic zone between the surface and the center of the specimen is apparent. When the amount of plasticity increases further (t_3) the difference becomes more pronounced. At the surface of the specimen the enlargement of the plastic zone in a 45° angle from the crack plane develops. The onset of plastic deformation at the surface of the structure accompanying

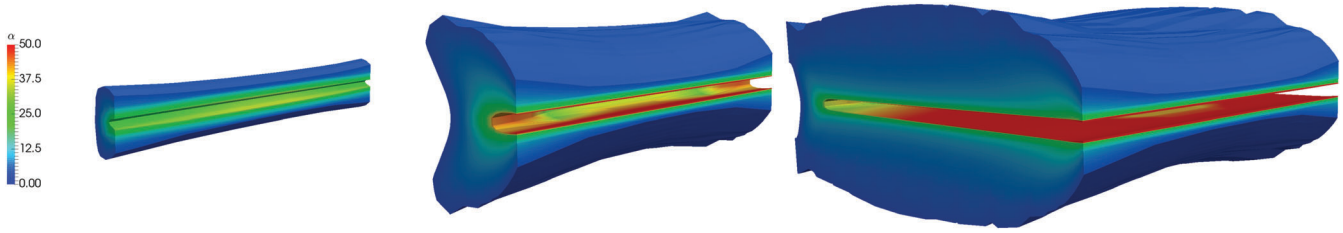

FIGURE 12 Plastic zone at simulation time t_2, t_3, and t_4 (from left to right) for $d = 0.4$

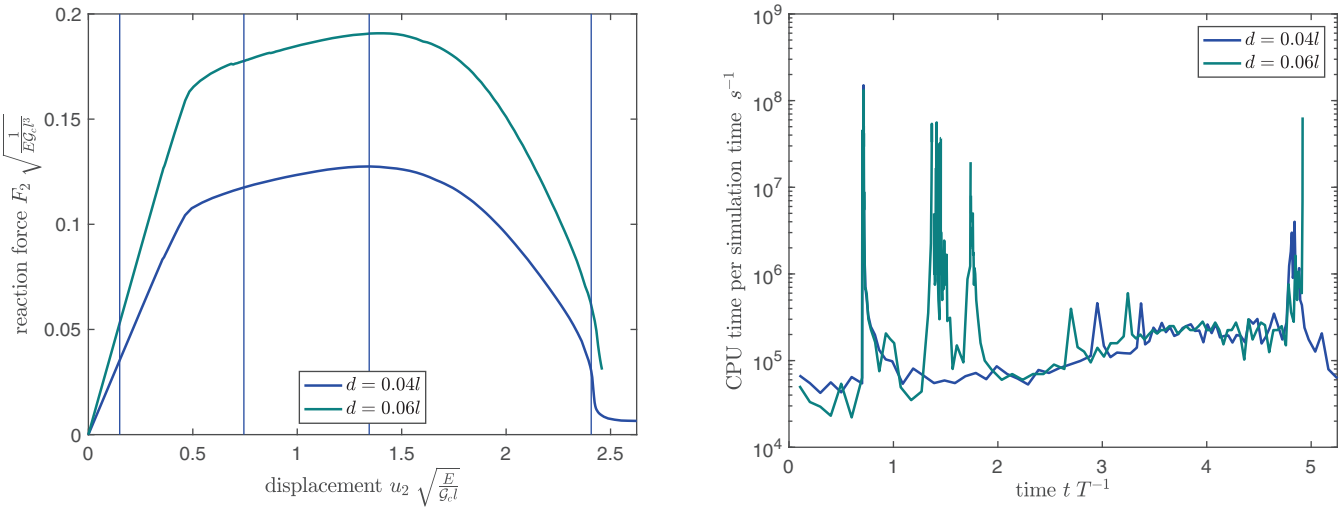

FIGURE 13 Load-displacement curve, where F_2 is the reaction force acting on the initially undamaged, right part of the structures x_2-surface and distribution of CPU time for simulation of a specimen of thickness $d = 0.4l$

the beginning of fracture in the center turns out to be the computationally most demanding part of the simulation, see Figure 13 on the right. Towards the end of the simulation further demanding parts emerge.

In order to assess the lateral expansion of the plastic zone in dependence of the position in direction of the crack front (x_3-direction), several slices at the instance, when the reaction force is almost at maximum level ($t = t_3$) are depicted in Figure 15. At the surface of the specimen the strongly shaped flanks in 45° angles from the crack propagation direction are noticeable. Thus, building up an extraordinary wide sickle resembling, concave shape in front of the crack tip. At $x_3 = 0.1$ the flanks are less pronounced, hence the extension of the plastic zone in x_2-direction is smaller and the concavity in front of the crack less pronounced. In the center of the specimen the shape is almost identical. The larger extension of the plastic zone in x_1-direction is due to fact, that the crack tip in the center has already propagated a little further than in the outer parts of the specimen. A similar picture unfolds for the specimen of thickness $d = 0.6l$ shown in Figure 16. The flanks and the concavity in front of the crack tip become less prominent the larger the distance from the surface. Even from $x_3 = 0.1$ to $x_3 = 0.2$ and further to the center a distinction is discernible. Compared to $d = 0.4l$ the surface feature seems to decay less strong, while due to the higher distance from the surface in the effect is almost fully decayed in the center. In case of the specimen with $d = 0.8l$ the trend holds also true, see Figure 17. At $x_3 = 0.2l$ concavity is still more pronounced compared to $d = 0.6l$, leading to the assumption that decay is even less strong. Like for $d = 0.6l$ the concavity is almost fully decayed in the center. However, the crack front and also the plastic zone in front of the crack tip are not perfectly symmetric as the slice at the surface with $x_3 = l$, where the concavity is almost not existent, shows. Hence, following the observations above, the discretization in x_3-direction in eight elements is not fine enough. As a conclusion from the observations regarding the discretization in direction of the crack tip a rough estimate of a suitable element length in x_3-direction of $n_3 \geq \frac{50}{4}\frac{d}{l}$ can be drawn. An element width of $d_{n3} = \frac{0.8l}{8} = 0.1l$ proved to be insufficient.

The trend of a decreasing size of the plastic zone towards the center of the specimen across the crack front observed here is related to the out-of-plane constraint, describing the structural obstacle against plastic deformation, due to the specimen dimension parallel to the crack front.[29] For the specimen with $d = 0.6l$ the out-of-plane constraint increases from the surface to $x_3 = 0.1$ significantly and slightly from $x_3 = 0.1$ to the center. In case of the smallest specimen thickness the out of plain constraint reaches its maximum value almost at $x_3 = 0.1$. Hence, the out-of-plane constraint at the center is still closer to that at the surface compared to the thicker specimen. A plastic zone in cylindrical shape where the cross section is largely dominated by the larger expansion at the surface for thinner specimens, while the cross section is mostly dominated by the

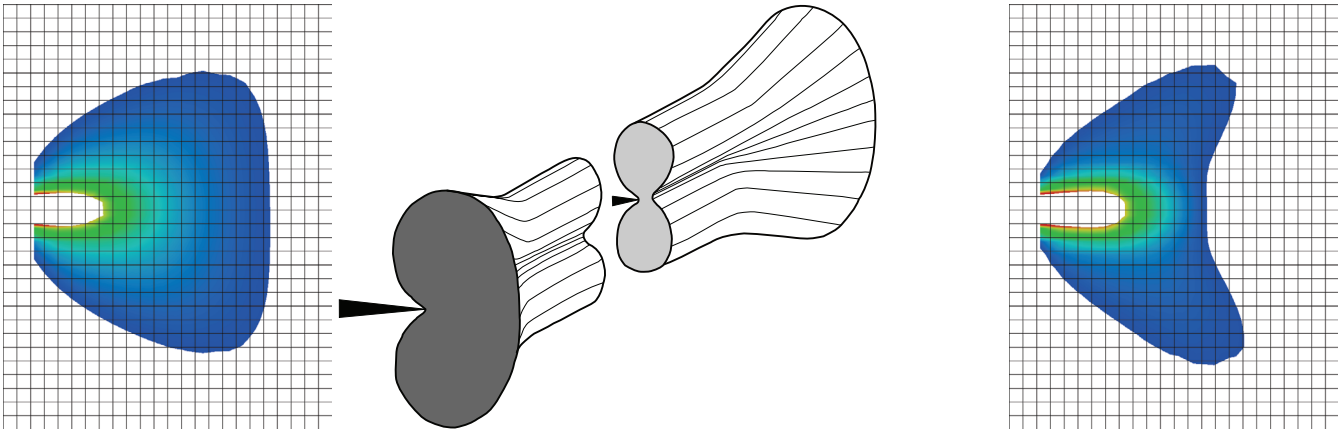

FIGURE 14 Slices of the plastic zone at the time when the reaction force is at maximum for a specimen with $d = 0.05$ approximating the plane stress state (left) and for a specimen under plane strain conditions (right). In the center a schematic sketch of the dog-bone model

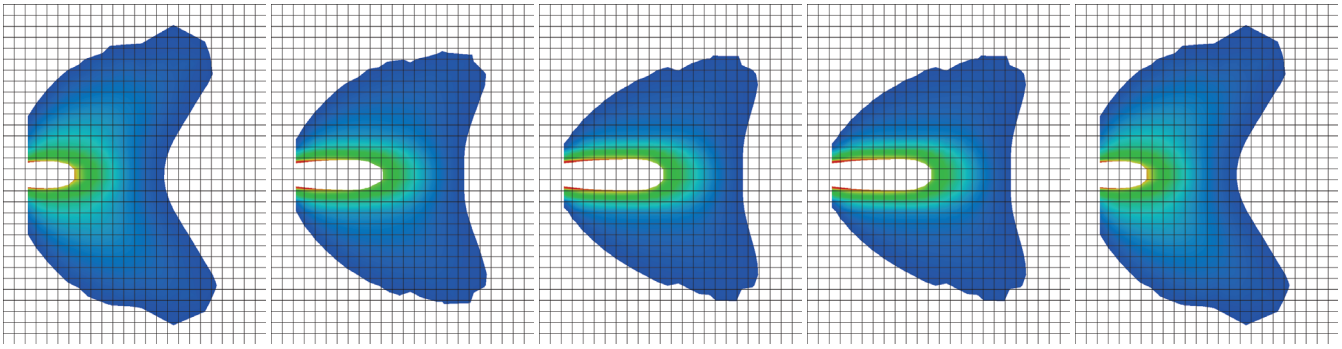

FIGURE 15 Slices at $x_3 = 0$, $x_3 = 0.1$, $x_3 = 0.2$, $x_3 = d/2$, and $x_3 = d$ (from left to right) of the plastic zone at simulation time t_3 for the specimen with $d = 0.4$

smaller extension in the center for thicker specimens is also observed.[2] The deminishing extension of the plastic zone at the crack front in direction of propagation as predicted in the dog-bone model, sketched in Figure 14 in the middle, where a plane stress state at the surface and plane strain state in the center of the specimen are predicted, however, is not observed. The scenario predicted in the dog-bone is observed neither by Fernandez Zuñiga et al.[2] nor by Kudari and Kodancha,[1] though. Hence the results at hand are in accordance with observations of the works named above. A comparison between the shapes of the plastic zone at the surface of the 3D specimen and the shape in a plane stress simulation (Figure 14 on the left) as well as between the shapes in the center of the specimen and the shape in a plane stress simulation (Figure 14 on the right) reveals an obvious distinction. Thus, neither a plane stress state on the surface nor a plane strain state in the center of the structure is established at the instance of time, when the reaction force is at its maximum in the 3D simulations. However, the shape of the crack front at this instance is already thumbnail like, while in the dog-bone model the crack front is assumed to be smooth. The front of plastic deformation on the other hand seems to be flat and thus, further ahead of the crack front on the surface then in the center, giving rise to the concave shape at the surface of the specimen in Figures 15–17. Furthermore, taking the size requirement criterion for K_{IC}-measurements into account, stating that the specimen thickness is large enough such that plane stress state dominated regions at the surface are negligible compared to plane strain state dominated regions inside the specimen if $d \geq 2.5\left(\frac{K_{\mathrm{IC}}}{\sigma_{\mathrm{Y}}}\right)^2$,[2] by applying the relation $\mathcal{G}_c = \frac{K_{\mathrm{IC}}^2(1-\nu)}{E}$ and assuming unaltered simulation parameters as above, a specimen thickness of $d \geq 3.3$ would be required. This is more then 5 times the largest specimen thickness considered, above.

4 | REMARKS AND OUTLOOK

In this contribution a phase field model for ductile fracture that is able to reproduce the main characteristics of ductile fracture on the one hand and gets along with a manageable amount of parameters, which can be related to experimentally measurable data, that, furthermore allows for the application of a monolithic solution scheme to solve the arising system of non-linear partial differential equations on the other hand, is enhanced. The implementation of a cubic degradation function rendered a reinterpretation of the plastic parameters unnecessary, but preserves the properties regarding its simplicity.

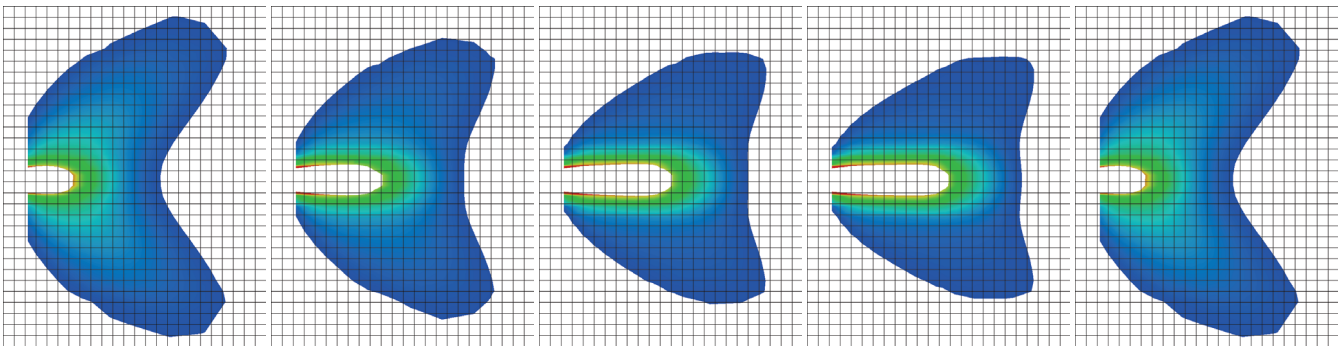

FIGURE 16 Slices at $x_3 = 0$, $x_3 = 0.1$, $x_3 = 0.2$, $x_3 = d/2$, and $x_3 = d$ (from left to right) of the plastic zone at simulation time t_3 for the specimen with $d = 0.6$

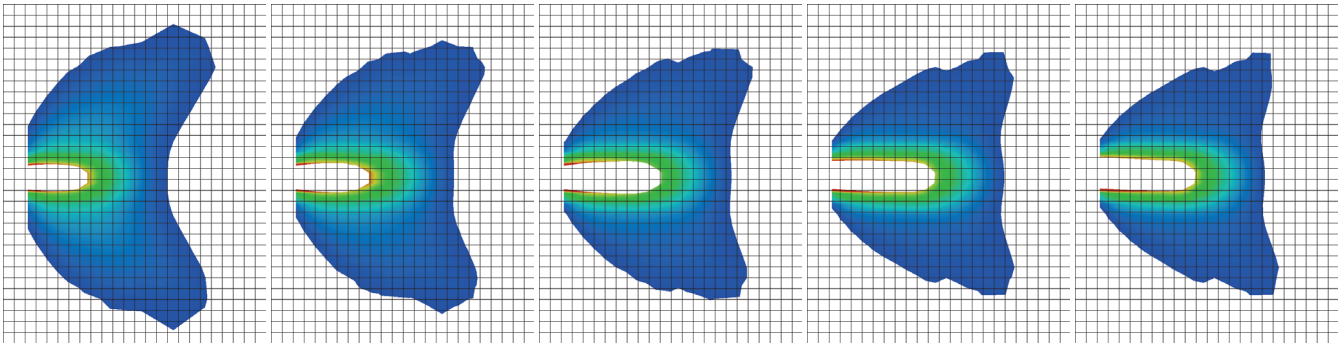

FIGURE 17 Slices at $x_3 = 0$, $x_3 = 0.1$, $x_3 = 0.2$, $x_3 = d/2$, and $x_3 = d$ (from left to right) of the plastic zone at simulation time t_3 for the specimen with $d = 0.8$

The model is tested by investigating the plastic zone at the crack front of a single notched tension specimen under tensile loading in 3D. In order to do so, an appropriate mesh consisting of eight node brick elements with a sufficiently fine resolved crack propagation zone was developed. Several differently refined meshes were tested. The necessary incorporation of transition elements in between regions with a coarser and regions with a finer mesh in order to establish a mesh conformity, turned out to impair the convergence of the solution scheme. A subsequent cleanup step provided only minor enhancement in terms of spent CPU time, but enhanced overall stability of the solution scheme. Moreover, it has to be stated, that the approach of prerefining the mesh in regions, where the crack is expected to grow requires the knowledge of the crack path in advance and thus, negating a substantial benefit of the phase field method. As on the other hand a sufficiently fine, unrefined mesh exceeds the available computational capacities, the only alternative is an adaptive remeshing procedure, which is both beyond the scope of this contribution and comprises the generation of new mesh parts during the simulation, hence, deteriorates another advantage of phase field models over conventional models and strongly complicates the implementation due to the required transfer of variables.

Alessi et al.[30] note that due to the application of identical degradation functions for the elastic strain energy and the hardening contribution plastic strain developed in regions, where the material is already fully broken, which might cause convergence issues. However, as the degradation function weakens the impact of α on the total plastic energy in the simulations considered here a saturation of the plastic energy is observed. Thus, from the authors' point of view no convergence issues can be explicitly related to the stated context.

The insights regarding the plastic zone at the crack front qualitatively conform with the results from Kudari and Kodancha[1] and Fernandez Zuñiga et al.[2] The out-of-plane constraint has a significant influence on the in-plane shape of the plastic zone. While for specimen of lower thickness the shape of the plastic zone is more dominated by the surface and is further extended in 45° angle to the crack propagation direction, in specimen of larger thickness the plastic zone tends to be more compact. Thus far, the results are in accordance with the classical dog-bone model. However, the dog-bone model predicts further plain strain states accompanied by almost no plastic deformation in front of the crack tip. This is neither observed in the work at hand nor in Kudari and Kodancha[1] and Fernandez Zuñiga et al.[2] and furthermore not expected as the thicknesses of the computed structure were to small. Furthermore, at the instant of time when the plastic zone is considered, the crack has formed a thumbnail shape already, while the dog-bone model assumes a flat crack front.

The computing power necessary to perform simulations in 3D is quite demanding. While a simulation with a mesh of 4560 elements in a single layer run for 40 h the simulation with a mesh of the same number of elements in five layers took 350 h. As structures with a thickness large enough to expect states close to plane stress at the surface and close to plane strain in the center would require a multiple of elements in x_3-direction, those simulations are beyond the scope of this approach. Measures to optimize the 3D simulations of ductile fracture might lead in several directions depending on where the focus is set, whether details on a smaller scale or phenomenological aspects on larger scales are of interest. More sophisticated mesh refinement procedures comprising for example, constrained Laplacian smoothing after performing the topological cleanup steps, require on the one hand attention to ensure that elements are not inverted, but promise to improve element quality dramatically.[28] The application of exponential shape functions, which approximate the shape of cracks better than conventional polynomial shape functions eases the requirement of mesh fineness.

ACKNOWLEDGEMENTS

The authors gratefully acknowledge support by the Deutsche Forschungsgemeinschaft in the Priority Program 1748 *Reliable simulation techniques in solid mechanics. Development of non-standard discretization methods, mechanical and mathematical analysis* under the project *Advanced Finite Element Modeling of 3D Crack Propagation by a Phase Field Approach*.

REFERENCES

[1] S. Kudari, K. Kodancha, in *17th European Conference on Fracture 2008: Multilevel Approach to Fracture of Materials, Components and Structures*, Vol. 1 **2008**, 530.
[2] D. Fernandez Zuñiga, J. F. Kalthoff, A. Fernandez-Canteli, J. Grasa, M. Doblare, in *17th European Conference on Fracture 2008: Multilevel Approach to Fracture of Materials, Components and Structures* **2005**.
[3] J. Besson, *SAGE Publications Ltd STM* **2010**, *19*, 3.
[4] N. Sukumar, N. Moës, B. Moran, T. Belytschko, *Int. J. Numer. Methods Eng.* **2000**, *48*, 1549.
[5] N. Moës, J. Dolbow, T. Belytschko, *Int. J. Numer. Methods Eng.* **1999**, *46*, 131.
[6] G. A. Francfort, J.- J. Marigo, *J. Mech. Phys. Solids* **1998**, *46*, 1319.
[7] B. Bourdin, G. A. Francfort, J.-J. Marigo, *J. Mech. Phys. Solids* **2000**, *48*, 797.
[8] J. Mediavilla, R. H. J. Peerlings, M. G. D. Geers, *Int. J. Numer. Methods Eng.* **2006**, *66*, 661.
[9] C. Miehe, F. Welschinger, M. Hofacker, *Int. J. Numer. Methods Eng.* **2010**, *83*, 1273.
[10] C. Miehe, M. Hofacker, F. Welschinger, *Comput. Methods Appl. Mech. Eng.* **2010**, *199*, 2765.
[11] H. Amor, J.-J. Marigo, C. Maurini, *J. Mech. Phys. Solids* **2009**, *57*, 1209.
[12] C. Kuhn, R. Müller, *Proc. Appl. Math. Mech.* **2008**, *8*, 10223.
[13] C. Kuhn, R. Müller, *Eng. Fract. Mech.* **2010**, *77*, 3625.
[14] M. Ambati, T. Gerasimov, L. De Lorenzis, *Comput. Mech.* **2015**, *55*, 383.
[15] A. Schlüter, A. Willenbücher, C. Kuhn, R. Müller, *Comput. Mech.* **2014**, *54*, 1141.
[16] M. Hofacker, C. Miehe, *Int. J. Numer. Methods Eng.* **2013**, *93*, 276.
[17] M. Hofacker, C. Miehe, *PAMM* **2012**, *12*(1), 173.
[18] H. Ulmer, M. Hofacker, C. Miehe, *Proc. Appl. Math. Mech.* **2013**, *13*, 533.
[19] F. P. Duda, A. Ciarbonetti, P. J. Sanchez, A. E. Huespe, *Int. J. Plast.* **2015**, *65*, 269.
[20] C. McAuliffe, H. Waisman, *Int. J. Plast.* **2015**, *65*, 131.
[21] M. Ambati, T. Gerasimov, L. De Lorenzis, *Comput. Mech.* **2015**, *55*, 1017.
[22] M. J. Borden, T. J. R. Hughes, C. M. Landis, A. Anvari, I. J. Lee, *Comput. Methods Appl. Mech. Eng.* **2016**, *312*, 130.
[23] C. Kuhn, T. Noll, R. Müller, *GAMM-Mitteilungen* **2016**, *39*, 35.
[24] M. J. Borden, C. V. Verhoosel, M. A. Scott, T. J. R. Hughes, C. M. Landis, *Comput. Methods Appl. Mech. Eng.* **2012**, *217-220*, 77.
[25] T. Simo, J. C. Hughes, Computational Inelasticity, Springer, New York **1998**.
[26] B. Bourdin, G. Frankfort, J.-J. Marigo, The Variational Approach to Fracture, Springer, Netherlands **2008**.
[27] R. Schneiders, Algorithms for Quadrilateral and Hexahedral Mesh Generation, **2011**.
[28] M. L. Staten, S. Benzley, M. Scott, *Eng. Comput.* **2008**, *24*, 241.
[29] H. Yuan, W. Brocks, *J. Mech. Phys. Solids* **1998**, *46*, 219.
[30] R. Alessi, M. Ambati, T. Gerasimov, S. Vidoli, L. De Lorenzis, in Comparison of Phase-Field Models of Fracture Coupled with Plasticity (Eds: E. Oñate, D. Peric, E. de Souza Neto, M. Chiumenti), Springer International Publishing, Cham **2018**, p. 1.

How to cite this article: Noll T, Kuhn C, Olesch D, Müller R. 3D phase field simulations of ductile fracture. *GAMM-Mitteilungen*. 2020;43:e202000008. https://doi.org/10.1002/gamm.202000008